Research Article

Low-temperature catalytic graphite blocks with high hardness and deformability

Jiahui Zhou[1,2], Daming Chen[3], Wenzheng Zhang[2]*, Yang Lyu[2], Chunlin Wang[1,2], Zhihong Han[1,2,4], Ao Chen[1], Yuhao Fang[1,2], Chiyu Wang[1], Yanju Gu[1], Hui Wang[1,2], Mingyi Tan[1*], Xinghong Zhang[1,2]

[1]National Key Laboratory of Science and Technology on Advanced Composites in Special Environments, Harbin Institute of Technology, Harbin 150001, Heilongjiang, China.

[2]Suzhou Laboratory, Suzhou 215124, Jiangsu, China.

[3]Beijing Institute of Aeronautical Materials, Beijing 100080, China.

[4]Suzhou Research Institute, Harbin Institute of Technology, Suzhou 215104, Jiangsu, China.

Correspondence to: Prof. Mingyi Tan, National Key Laboratory of Science and Technology on Advanced Composites in Special Environments, Harbin Institute of Technology, Harbin, 150001, ASS Prof China. E-mail: tanmy@hit.edu.cn; Prof. Wenzheng Zhang, Suzhou Laboratory, Suzhou, 215124, PR China. E-mail: zhangwz@szlab.ac.cn

Received: 19 May 2026 | Approved: 28 May 2026 | Online: 28 May 2026

Abstract

Graphitized carbon is highly attractive for its excellent electrical and thermal conductivity, structural stability, and mechanical reliability, making it crucial for applications such as aerospace thermal protection and thermal management systems. Currently, producing highly graphitized carbon predominantly relies on petrochemical

precursors and requires energy-intensive ultra-high-temperature processing. As a sustainable alternative, sugar-derived carbon is highly desirable; however, its application is severely limited by its hard-to-graphitize nature and low carbon yield. To address this challenge, we propose a low-temperature catalytic graphitization strategy by introducing a ferric nitrate catalyst into a glucose hydrogel precursor via a sol-gel route. This method enables the molecular-level uniform dispersion of Fe species and the in situ formation of highly dispersed catalytic centers during pyrolysis. Remarkably, this approach significantly lowers the energy barrier for structural transformation, allowing the sugar-derived carbon treated at merely 1,400 °C to achieve a graphitization degree comparable to that of the uncatalyzed sample treated at 2,400 °C. More importantly, the catalytic process not only improves structural ordering but also induces a highly curved, crosslinked, and interlocked graphitic topology, which effectively suppresses basal-plane sliding. Consequently, the material achieves both high graphitization and superior micromechanical properties, exhibiting 1.5 times higher hardness and 2 times higher micro/nano-compressive strength compared to the uncatalyzed material at a similar graphitization level. This work provides an efficient and sustainable strategy for the low-cost and energy-saving fabrication of high-performance biomass-derived graphitic carbon.

Keywords: Sugar-derived carbon, catalytic graphitization, topological graphitic network, micromechanical properties

INTRODUCTION

Graphitized carbon is highly attractive for advanced carbon materials because of its high electrical and thermal conductivity, structural stability, and mechanical reliability. These features are particularly important for applications that require efficient transport capability together with structural robustness, such as aerospace thermal protection, thermal management, and high-performance graphitic carbon blocks[1-4]. Consequently, the efficient and scalable fabrication of highly graphitized carbon has become an

important topic in carbon materials research.

At present, highly graphitized carbons are still produced mainly from petrochemical precursors (e.g. petroleum coke and pitch), through carbonization followed by ultrahigh-temperature graphitization (typically above 2,800 °C)[5-7]. Such severe processing conditions lead to high energy consumption, high production cost, and potential damage to the structural integrity of carbon framework. To develop sustainable and low-cost alternatives, sugar-derived carbon has emerged as a highly attractive candidate due to its abundant, renewable nature and compatibility with hydrogel chemistry for morphology regulation. However, the development of sugar-derived graphitic carbon has historically been hindered by two critical bottlenecks: inherently low carbon yield and extreme difficulty in graphitization[9]. While recent advances in hydrogel-network engineering and precursor regulation have successfully addressed the low-carbon-yield problem, the fundamental issue of poor graphitizability remains unresolved[10]. After pyrolysis, sugar precursors typically form a highly crosslinked, intrinsically disordered carbon framework with abundant defects[5,8]. The restricted atomic mobility within this rigid matrix makes the rearrangement into extended graphitic stacking extremely difficult, even at elevated temperatures. Thus, finding a targeted solution to break the graphitization barrier of sugar-derived carbon is highly desired.

Catalytic graphitization provides a promising strategy to overcome this structural limitation. By introducing ransition metal catalysts (such as Fe, Ni, or Co) into disordered carbon precursors, the activation barrier for carbon reconstruction can be significantly reduced[11-16]. Among them, Fe-based catalysts are particularly attractive because of their low cost, high catalytic activity, and strong interaction with carbon. Through dissolution-precipitation and diffusion-assisted mechanisms, Fe/Fe-C intermediates can promote the transformation of amorphous carbon into ordered graphitic structures at temperatures much lower than conventional thermal

graphitization. However, applying traditional catalytic graphitization to highly crosslinked sugar carbon matrices still faces significant challenges. Conventional approaches relying on direct mixing or impregnation often lead to severe catalyst aggregation and non-uniform catalytic sites[17,18]. Furthermore, while most previous studies focus primarily on improving the overall degree of graphitization, how catalytic species regulate the spatial organization, curvature, and topological connectivity of graphitic domains at the micro/nanoscale—which ultimately dictates the macroscopic mechanical properties—has received much less attention.

To address these challenges, we report a ferric-nitrate-enabled in situ catalytic graphitization strategy specifically designed to overcome the graphitization bottleneck of sugar hydrogel-derived carbon. Ferric nitrate was selected as a water-soluble Fe precursor and homogeneously incorporated into the glucose hydrogel network through a sol-gel route. This design ensures the in situ formation of highly dispersed Fe-containing catalytic centers during pyrolysis, effectively suppressing catalyst aggregation and maximizing the atomic-level contact between Fe species and the rigid disordered carbon framework. As a result, the intrinsically difficult-to-graphitize sugar-derived carbon achieves substantial graphitic reconstruction at significantly reduced temperatures (1,400 °C). More importantly, this catalytic process does not merely increase the crystallinity, but induces a curved, crosslinked, and structurally constrained graphitic microstructure. By combining thermal evolution analysis, structural characterization, nanoindentation, and in situ micropillar compression, this work reveals how Fe-catalyzed structural reconstruction governs the micromechanical response of sugar-derived graphitic carbon. This strategy not only bridges the graphitization gap for sugar-derived systems but also provides a targeted pathway for the low-temperature fabrication of sustainable, high-performance graphitic carbon blocks for advanced engineering applications.

EXPERIMENTAL SECTION

Materials

Anhydrous ethanol, analytically pure. Tianli Chemical Reagents Ltd. Tianjin (China). Ultrapure water, Aladdin Scientific Corp. Shanghai (China).Ferric nitrate nonahydrate ($Fe(NO_3)_3 \cdot 9H_2O$, 99.9%) and α-Ketoglutaric acid ($C_5H_6O_5$,99%) were purchased from Aladdin Reagent (Shanghai) Co. Acrylamide (C_3H_5NO, AR), purchased from Tianjin Comio Chemical Reagent Co, LTD. Glucose monohydrate ($C_6H_{12}O_6 \cdot H_2O$, 99%) N,N'-Methylene-bis-acrylamide ($C_7H_{10}N_2O_2$,99%) and was purchased from Beijing J&K Scientific Co, LTD. All materials used in this work were of commercial grade and applied without further purification.

Preparation of carbonaceous materials with enhanced graphitization properties

First, 77 g of glucose hydrate was mixed with 23 g of deionized water. Then, N,N'-methylene bis-acrylamide (1 wt% relative to glucose) and acrylamide (20 wt% relative to glucose) were successively added to form a uniform precursor solution. Next, anhydrous ferric nitrate was introduced as a graphitization catalyst, and the mixture was further dispersed through stirring and ultrasonic treatment. After adding α-ketoglutaric acid (0.7 wt% relative to glucose) as a photoinitiator, the precursor solution was poured into a mold and photopolymerized under ultraviolet irradiation to obtain the sugar hydrogel.

The obtained hydrogel was then subjected to a gradual low-temperature stabilization/pre-graphitization treatment in air to ensure complete dehydration and structural solidification, followed by carbonization and catalytic graphitization in a tube furnace under an argon atmosphere. By varying the content of ferric nitrate in the precursor, a series of X-Fe/GC samples were obtained, where X = 0.05, 0.1, 0.5 and 1.0 wt% representing the iron content in the final carbonaceous material. Furthermore, in order to conduct a control experiment, sugar water gel carbon (SC) without catalyst was prepared during the experiment.

Characterization

X-ray diffraction (XRD) was carried out on a Rigaku Smartlab 3 kW diffractometer (Japan) to identify the phase composition, crystal structure, and interplanar spacing of the samples. Scanning electron microscopy (SEM) images were acquired using an FEI Helios Nanolab 600i microscope (USA) operated at an accelerating voltage of 20 kV. Fourier transform infrared (FTIR) spectra were recorded on a PerkinElmer 2,000 spectrometer (USA). Transmission electron microscopy (TEM) and high-resolution TEM (HRTEM) observations were performed on an FEI Tecnai G2-F30 TEM at an accelerating voltage of 200 kV. Raman spectra were measured on a Renishaw spectrometer with a 532 nm laser excitation source. The micromechanical properties of the samples were tested via a nanoindentation system (Anton Paar NHT2, Austria). In-situ SEM compression and tensile tests were conducted on an FEI Helios Nanolab 600i microscope integrated with a Hysitron PI-88 mechanical testing stage, allowing direct observation of crack propagation during deformation. Quantitative analysis of Fe element in the samples was performed using an inductively coupled plasma optical emission spectrometer (ICP-OES, Thermo Fisher iCAP PRO, USA). The thermal evolution behavior was characterized by thermogravimetric analysis (TGA) on a Netzsch STA449F3 instrument coupled with a Netzsch QMS 403Q mass spectrometer (Germany) under an argon atmosphere at a heating rate of 5 °C min^{-1}. The surface chemical composition and chemical states were analyzed by X-ray photoelectron spectroscopy (XPS) on a Thermo Scientific K-Alpha spectrometer (USA).

RESULTS AND DISCUSSION

Synthesis and thermal conversion of X-Fe/GC

The formation of X-Fe/GC is based on the water gel precursor developed by our team using the thermal decomposition carbon of the sugar water gel as the foundation[1,2,19-21]. Compared with the residual carbon content of 33.32% in glucose powder, the final carbon yield of the sugar water gel after thermal decomposition can reach 83.03%. This improvement is mainly attributed to the synergistic effect between the

high-concentration glucose solution and the AM network. In this process, the three-dimensional AM network confines glucose molecules during the gelation process and stabilizes the precursor structure through hydrogen bond interactions. During the pre-carbonization process, glucose undergoes dehydration and caramelization reactions, forming furfural derivatives and further polymerized caramel substances, rather than directly escaping as volatile carbon gases. At the same time, the local high-pressure environment generated by the contraction of the AM network can inhibit gas generation and uncontrollable foaming, thereby reducing carbon loss and forming a more compact carbon structure[19]. Subsequently, it undergoes carbonization and catalytic graphitization processes. As illustrated in Figure 1A, acrylamide and bis-acrylamide are introduced into a highly concentrated glucose solution to construct the precursor network, followed by the addition of ferric nitrate to obtain the Fe-containing precursor. Ferric nitrate was selected because it can be introduced into the hydrogel system in a uniform solution state without introducing additional impurity elements into the precursor framework based on C/H/O/N. This precursor design is crucial, as it effectively inhibits catalyst aggregation and provides uniformly distributed catalytic sites during the subsequent heat treatment.

The dispersion state of Fe in the precursor-derived carbon was examined by SEM and EDS mapping. As shown in Figure 1B-D, Fe is uniformly distributed throughout the carbon matrix without obvious agglomeration. This result confirms that the solution-based incorporation route enables effective dispersion of Fe species at the molecular level, maximizing the contact between the catalytically active species and the disordered carbon framework during thermal conversion. Such homogeneous dispersion is particularly important for difficult-to-graphitize sugar-derived carbon, since localized catalyst clustering would limit the spatial uniformity of graphitic reconstruction.

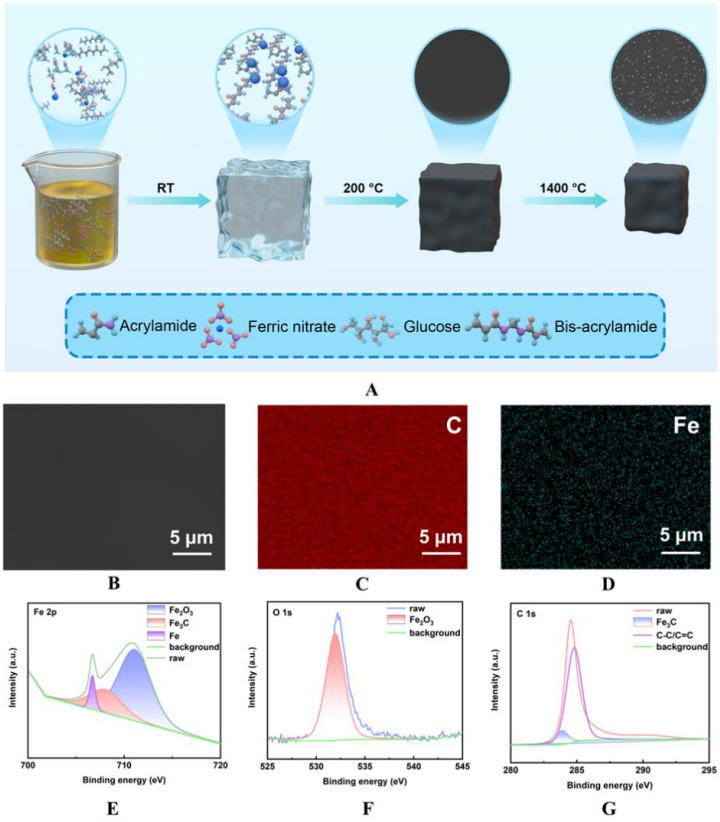

Figure 1. The low-temperature pyrolysis carbonization process for preparing graphite from sugar-water gel and the component characterization. A: Schematic diagram of the process flow for preparing X-Fe/GC materials by combining sol-gel method, pre-carbonization, carbonization and graphitization treatments; B-D: SEM images of the 0.5-Fe/GC samples and corresponding elemental EDS cross-sectional scans of C and Fe elements; E-G: XPS analysis of 0.5-Fe/GC after pre-carbonization; E: Fe 2*p* orbitals spectrum; F: O 1*s* orbital spectrum; G:C 1*s* orbital spectrum.

To further clarify the chemical evolution of Fe during precursor conversion, XPS analysis was performed on the pre-carbonized Fe-containing sample. The Fe 2p spectrum [Figure 1E] reveals multiple Fe-related species, with characteristic contributions corresponding to Fe_2O_3, Fe_3C, and metallic Fe. Additionally, the O 1s spectrum [Figure 1F] confirms the presence of iron oxide species, while the C 1s spectrum [Figure 1G] exhibits a characteristic Fe_3C-related peak. These results indicate that ferric nitrate does not remain in its initial state during thermal treatment, but instead undergoes decomposition, reduction, and carbide-related transformations. Therefore,

prior to the final graphitization stage, Fe has already evolved into chemically active intermediates that directly participate in carbon reconstruction.

Figure 2 summarizes the thermal conversion behavior and bonding-state evolution of SC and Fe/GC during heat treatment. As shown in Figure 2A, both samples undergo substantial mass loss in the low-temperature region due to dehydration and initial carbonization. Notably, the Fe-containing sample exhibits a lower mass loss than SC at low temperature, but a more pronounced mass-loss feature in the high-temperature region, eventually resulting in a larger total mass loss after full heat treatment. The suppressed low-temperature mass loss of 0.5-Fe/GC suggests that Fe participates in the retention of carbon- and oxygen-containing species, likely through the formation of Fe-O and Fe-C related intermediates. In this sense, Fe may exert a carbon/oxygen fixation effect in the early stage, delaying the release of part of the volatile species and shifting part of the conversion process to higher temperatures.

The TG-MS results further clarify the nature of this high-temperature evolution. As shown in Figure 2B, characteristic signals at m/z = 12, 44, 48, and 64 become evident above ~1,000 °C. Among them, the strong enhancement of the m/z = 48 signal indicates the formation of carbon-cluster-related fragments during high-temperature treatment[22]. To verify this assignment, isotope analysis was performed using the corresponding m/z = 49 signal. As shown in Figure 2D and Figure 2E, the m/z = 49 signal remains much weaker than m/z = 48, and the relative intensity of m/z = 49 with respect to m/z = 48 is on the order of a few percent, which is consistent with the expected isotopic abundance of a C_4-containing fragment[23]. This provides additional support for assigning m/z = 48 to carbon-cluster species rather than Fe-related volatile products. Meanwhile, no sustained enhancement of Fe-related volatilization signals is observed, indicating that the high-temperature process is dominated by dynamic bond breaking and reconstruction of the carbon framework rather than extensive evaporation of Fe species[24].

The temperature-dependent ICP result shown in Figure 2C reveals that the Fe content first increases and then decreases with increasing temperature. The initial increase is mainly associated with the progressive removal of volatile organic components,

whereas the subsequent decrease suggests that Fe species undergo continuous evolution during heat treatment, including migration, encapsulation, or partial loss. Combined with the lower low-temperature mass loss of the Fe-containing sample, these results suggest that Fe does not remain inert in the carbon matrix, but actively participates in the redistribution and retention of carbon- and oxygen-containing species during the early stage and in their subsequent high-temperature reconstruction[12,25].

The evolution of carbon bonding states was further examined by C 1s XPS analysis. As shown in the spectra for 0.5-Fe/GC [Figure 2F] and SC [Figure 2G], both samples evolve toward more ordered carbon structures with increasing temperature; however, the Fe-catalyzed sample exhibits a much more pronounced increase in the C = C component and a clearer π-π* feature. This trend is quantitatively reflected in Figure 2H, where the sp^2/sp^3 ratio of 0.5-Fe/GC increases much more rapidly than that of SC, especially above 1,200 °C. These results indicate that Fe catalysis markedly accelerates the transformation of disordered sugar-derived carbon into sp^2-rich conjugated carbon[12,26].

Taken together, the results in Figure 2 show that Fe-catalyzed graphitization is not merely a temperature-lowering effect. Instead, Fe redistributes the conversion pathway of sugar-derived carbon by suppressing part of the low-temperature volatilization through carbon/oxygen fixation and promoting more intensive reconstruction at higher temperatures. This behavior provides indirect support for the subsequent carbide-related transformation pathway, because the early retention of carbon- and oxygen-containing species in Fe-related intermediates is expected to facilitate later Fe-C interaction, carbide evolution, and graphitic reorganization.

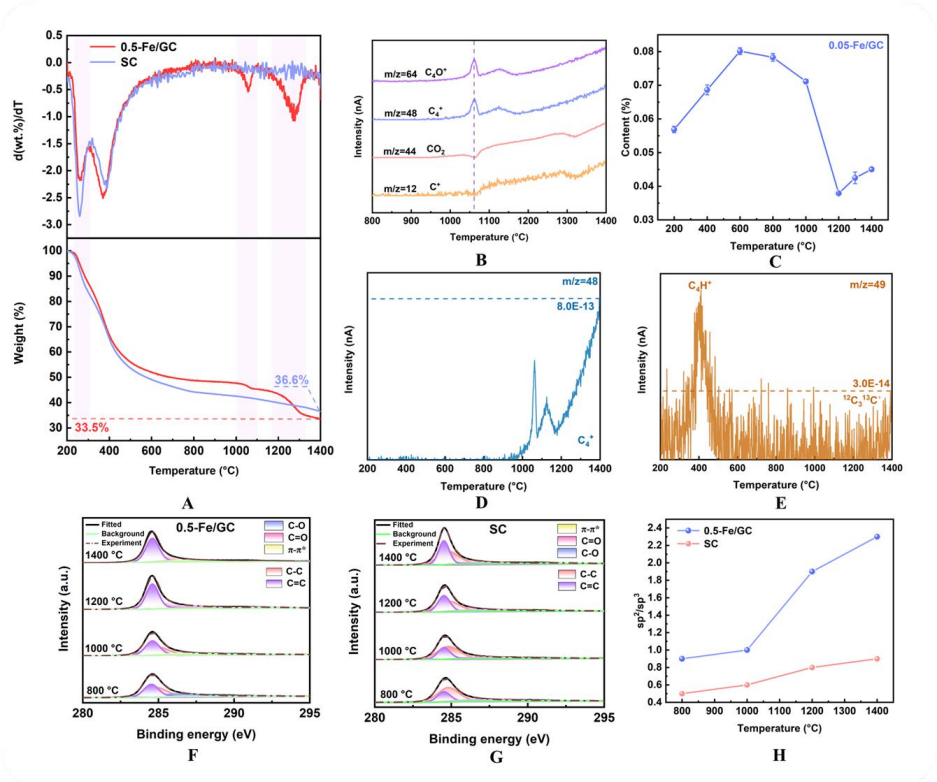

Figure 2. Thermal conversion and carbon bonding evolution of SC and Fe/GC. A: TG/DTG curves; B: TG-MS profiles of representative fragments. C:Temperature-dependent Fe content from ICP.D-E: m/z = 48 and the corresponding isotope-related m/z = 49 signal; F,H: Temperature-dependent C 1*s* XPS spectra of 0.5-Fe/GC and SC. G: sp^2/sp^3 ratio as a function of temperature.

In order to further reveal the regulatory effect of ferric nitrate content on the microstructure of sugar hydrogel-derived carbon, Raman and XRD characterizations were conducted. Figure 3A shows the Raman spectra of samples with varying iron contents. All samples exhibit characteristic D and G bands near 1,350 cm^{-1} and 1,580 cm^{-1}, respectively. The pristine SC sample displays broad and highly overlapping D and G bands, with an almost indistinguishable 2D band (around 2,700 cm^{-1}), demonstrating the typical features of highly disordered hard carbon. With increasing Fe content, the G band becomes significantly sharper, and the intensity of the 2D band progressively emerges and intensifies, confirming that the presence of Fe induced the transformation of the carbon framework from a disordered state to an ordered graphitic lattice. As shown in Figure 3B, as the Fe concentration increases from 0 to 1 wt.%, the I_D/I_G value

decreased significantly from 1.42 to 0.23. According to the Tuinstra-Koenig relationship[27,28], I_D/I_G is inversely proportional to the lateral size L_a of the graphitic crystallites. The calculated La increases dramatically from an initial 4.3 nm to approximately 19.8 nm, providing solid evidence that Fe catalysis significantly promotes the lateral growth of graphitic domains.

$$L_a = C(\lambda)/(I_D/I_G) \qquad (1)$$

The XRD spectra in Figure 3C further confirm this structural evolution. For the un-catalyzed sample treated at 1,400 °C (1,400-SC), the (002) diffraction peak is wide and weak, indicating poor stacking order and low crystallinity. The (002) peak of the sample (2,400-SC) with a higher heat treatment temperature (2,400 °C) is significantly sharper, from which it can be seen that increasing the heat treatment temperature can promote the rearrangement of carbon atoms and increase the crystallinity of graphite. In contrast, introducing iron at 1,400°C significantly accelerates this ordering process. As the iron content increases, the (002) peak gradually shifts to a higher angle, and its full width at half maximum (FWHM) significantly decreases, indicating a reduction in interlayer spacing and an increase in stacking coherence. It is notable that the XRD spectrum of 1,400-0.5-Fe/GC is highly similar to that of 2,400-SC, suggesting that the iron catalytic effect enables the sugar-derived carbon to achieve graphite-like state at 1,400°C, otherwise, it requires an extremely high temperature treatment to achieve this. As shown in Figure 3D, the interlayer spacing $d_{(002)}$ of 1,400-SC is 0.361 nanometers, reflecting the typical vortex structure of the carbon derived from sugar that is difficult to graphiteize. After adding iron, $d_{(002)}$ significantly decreases and reaches approximately 0.340 nanometers in 0.5-Fe/GC, close to the value of graphite carbon[29,30]. Correspondingly, the graphiteification degree calculated from SC is nearly 0%, increasing to approximately 45%-50% in 0.5-Fe/GC. Further increasing the iron content to 1.0% wt% only leads to a slight improvement in $d_{(002)}$ and graphiteification degree, indicating that once a sufficiently continuous iron catalytic network is established, the

catalytic effect will tend to saturate. Therefore, choosing 0.5% wt% of iron as the representative optimized component is because it achieves significant graphiteification while avoiding unnecessary catalyst overloading, possible iron aggregation, and limited additional structural benefits. These results indicate that iron does not merely act as an additive but effectively lowers the activation energy for carbon rearrangement and promotes graphite formation at lower temperatures.

$$g=\frac{0.3440-d_{(002)}}{0.3440-0.3354}\times 100\% \qquad (2)$$

This structural ordering is also visually corroborated by the HRTEM image of 0.5-Fe/GC [Figure 3F]. The sample exhibits highly ordered lattice fringes with an interplanar spacing of approximately 0.340 nm, closely matching the XRD results and approaching the value of ideal graphite (0.335 nm).Furthermore, the chemical state of carbon was investigated by XPS. As shown in Figure 3E, the C 1s spectrum is deconvoluted into multiple components. Compared with SC, the Fe/GC sample exhibits a markedly enhanced sp^2 hybridized carbon peak (C = C, ~284.5 eV) and a highly distinct π-π satellite peak (~291 eV), both of which are decisive indicators of an extended conjugated graphitic structure.

Concurrently, the relative intensity of oxygen-containing functional groups (C-O and C = O) is significantly reduced, indicating thorough deoxygenation during high-temperature reconstruction[26,31,32]. The substantial increase in the $sp^2/(sp^2+sp^3)$ ratio further confirms the catalytic effect of Fe on sp^2 lattice formation, perfectly aligning with the Raman and XRD analyses.

It is worth noting that when the iron concentration reaches 0.5 wt.%, the improvement of graphiteification indicators (I_D/I_G and $d_{(002)}$) tends to level off. This suggests that 0.5 wt.% Fe is the optimal threshold required to form a pervasive catalytic percolation network throughout the hydrogel-derived matrix. Below this threshold, the catalytic

sites are insufficient to drive widespread reconstruction; above this threshold, the marginal contribution to lattice perfection diminishes, and excessive metal content could potentially induce severe agglomeration, generating larger inactive carbide clusters or leaving detrimental metallic impurities in the final carbon block. Therefore, 0.5 wt.% was selected as the optimal catalyst concentration for subsequent micromechanical evaluations, as it balances superior graphitic crystallinity with the preservation of structural integrity.

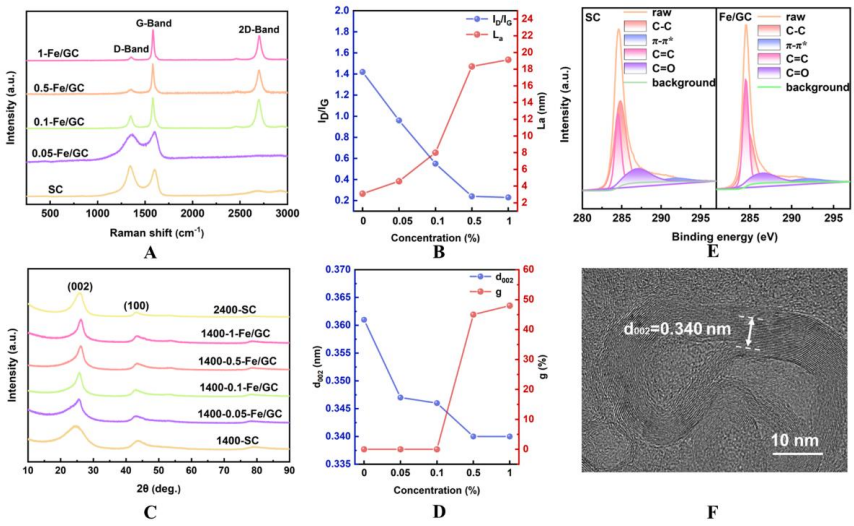

Figure 3. The influence of iron content on the degree of graphitization and the evolution of microstructure. A: Comparison of Raman spectra of samples with different iron contents; B: The variation trend of the ratio I_D/I_G and the transverse size L_a of graphite microcrystals with iron concentration; C: XRD patterns of samples with different iron contents; D: The functional relationship between the interlayer spacing $d_{(002)}$ and the calculated graphiteification degree (g) with respect to the iron concentration; E: High-resolution XPS spectra of C 1*s* for SC and Fe/GC samples; F: TEM image of 0.5-Fe/GC.

Structural evolution and catalytic graphitization mechanism

In the presence of Fe, the graphitization mechanism of carbon derived from the pyrolysis of sugar hydrogels is schematically illustrated in Figure 4. Based on the results of TEM observations and the elemental mapping [Figures 4A-E], a typical

catalytic graphitization process following the dissolution - diffusion - precipitation mechanism can be proposed[33].

During the initial pyrolysis stage, the sugar hydrogel undergoes dehydration and carbonization processes, thereby forming an amorphous carbon matrix. Meanwhile, the Fe precursor decomposes at high temperatures into iron oxides, which are subsequently reduced to metallic iron nanoparticles. From the elemental mapping [Figures 4C and 4D], it can be seen that carbon is uniformly distributed throughout the matrix, while Fe is concentrated and aggregated, indicating the formation of independent Fe nanoparticles dispersed within the carbon framework.

At high temperatures, these iron nanoparticles act as active catalytic centers for graphitization. The carbon atoms from the surrounding amorphous carbon around are thermally activated and gradually dissolve into the Fe nanoparticles due to the strong interaction between Fe and C. As the carbon concentration within the Fe particles increases, the system reaches an oversaturation state. Consequently, carbon atoms precipitate from the Fe surface and recombine to form thermodynamically favored graphite structures bonded by sp^2 bonds.

HRTEM image [Figure 4E] clearly shows distinct lattice fringes corresponding to the graphite layers, confirming the formation of ordered graphite domains. It is notable that these graphite layers are mainly observed near the iron nanoparticles, indicating that the graphitization process is highly localized and catalyst-driven.

As this process continues, the graphite layers grow along the surface of the Fe nanoparticles, forming a core-shell type Fe-graphite structure and partially graphitized carbon regions [Figure 4F]. This interface growth phenomenon further confirms the dissolution-precipitation mechanism[14].

Concurrently, some Fe species drive catalytic graphitization according to the carbide formation-decomposition mechanism [Figure 4G]. The so-called carbide-mediated mechanism refers to the reaction of catalytic components with the carbon matrix at high temperatures to form corresponding carbides[34,35]. When the temperature is further increased above the decomposition temperature of the carbides, they undergo decomposition reactions to generate elemental catalyst components and carbon; the newly formed carbon precipitated during this decomposition possesses a highly ordered graphitic structure. The elemental catalyst regenerated by the decomposition diffuses along the surface of the carbide particles toward the disordered carbon side, continuing to react with the disordered carbon to form new carbides and consume the amorphous matrix. As the carbide particles migrate, this process repeats itself, thereby continuously converting the disordered carbon into graphitic crystallites and substantially increasing the overall degree of graphitization of the material.

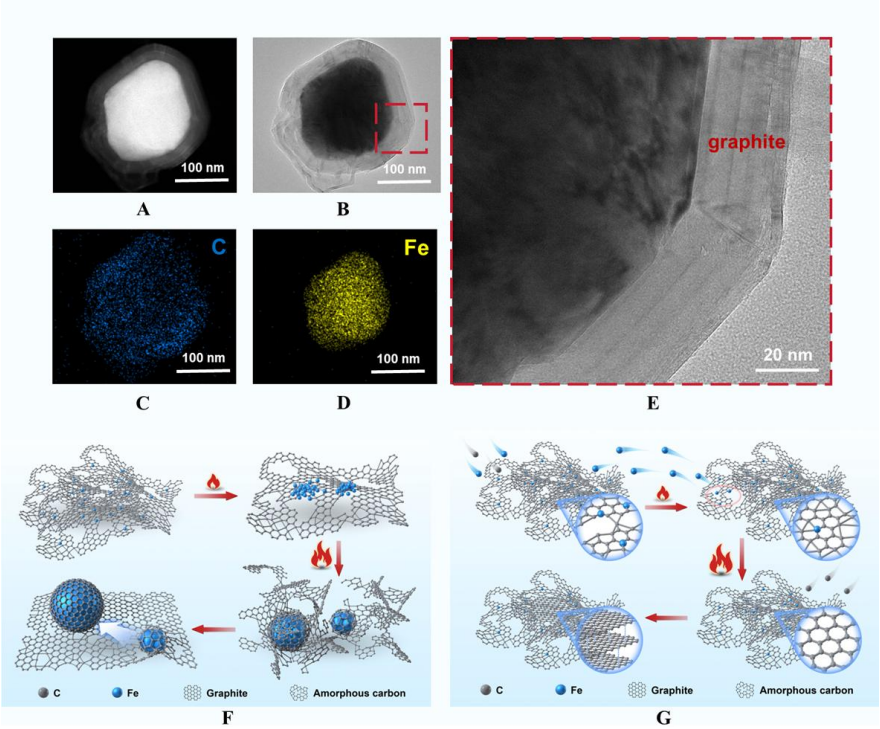

Figure 4. Model of the iron-induced graphitization mechanism. A-E: Analysis of the morphology and composition of the catalytic core. A-B: TEM/STEM images of the core-shell structure C-D: Distribution map of C and Fe elements in a single particle; E:

High-resolution lattice fringes at the iron/graphite interface; F: Schematic diagram of the dissolution-diffusion-precipitation mechanism; G: Schematic diagram of the decomposition and migration mechanism of carbides.

Structure-dependent micromechanical properties

The Fe-catalyzed induction strategy not only increases the graphitic ordering of sugar hydrogel-derived carbon, but also fundamentally changes the morphology and arrangement of the graphitic domains. As revealed by the TEM observations [Figure 5A-C], the original disordered carbon matrix is reconstructed into a highly curved, wrinkled, and topologically interlocked graphitic network rather than a conventional parallel lamellar graphite-like structure. Such a catalyst-induced architecture is mechanically important because the local arrangement of graphitic domains directly governs how the material accommodates concentrated stress. In particular, the curved and spatially constrained graphitic units can physically restrict facile interlayer sliding and provide a more effective three-dimensional load-transfer framework. Therefore, in the present work, the key issue is not simply whether graphitization is enhanced, but how the reconstructed graphitic architecture influences the local mechanical response[36]. This microscopic structural feature directly explains the mechanical performance retention observed in the nanoindentation experiments [Figure 5D and E]: the material maintains an intrinsic hardness of approximately 3.5 GPa and an excellent elastic modulus despite a significant increase in sp^2 hybridization content. This robustnesss is attributed to the reduction in the density of internal statistical defects (such as micropores and microcracks) at the micro/nanoscale. Moreover, the continuous sp^2 network formed by the catalyzed graphitization can more effectively hinder the initiation of dislocations or cracks within a small volume. Further in situ micropillar compression analysis [Figure 5F and G] deeply elucidates the decisive influence of this topological network on the material's service behavior. It is worth mentioning that Fe-containing particles were intentionally avoided during site selection, such that the measured behavior mainly represents the intrinsic mechanical contribution of the reconstructed carbon framework. The test results show that this microscopic configuration, composed of flexible curved graphene rings, acts as a mechanical "nano-spring": when an external load is applied, these curved layers can efficiently absorb a large amount of strain energy through local coordinated folding, reversible

rotation, and stress redistribution, thereby avoiding catastrophic instability and accumulation of stress at microcrack tips[37,38]. This energy dissipation mechanism endows the material with the extraordinary large-deformability, allowing it to maintain structural integrity under an extreme engineering strain of over 30%. And at the same level of graphitization, its hardness is 1.5 times higher than that of the un-catalyzed material, and its micro/nano-level compressive strength is 2 times higher[1]. Additionally, driven by the significant size effect, when the micropillar diameter is reduced to 0.5 μm, its compressive strength jumps to approximately 7.5 GPa due to the decreased probability of incorporating critical internal defects. In conclusion, the catalyzed graphitization path proposed in this study achieves a synergistic combination of “high graphitization degree” and “high mechanical performance”, breaking the traditional perception that crystallinity and robust mechanical behavior cannot be achieved simultaneously in sugar-derived carbons. The catalyst not only promotes the rearrangement of carbon atoms but also induces the formation of a highly cross-linked nanoscale graphitic network, which maintains hardness while enhancing deformability. The graphitized regions act as microscopic “dampeners”, effectively buffering external loads through interlayer shear and localized rotation, giving the material the ability to maintain structural integrity under extreme compression. The “rigid-flexible” topologically crosslinked nano-network confirmed by TEM successfully overcomes the long-standing trade-off relationship between hardness and deformability in carbon materials. This unique microstructural reconstruction provides solid physical evidence for the exceptional comprehensive mechanical performance of the sugar-derived graphitic carbon.

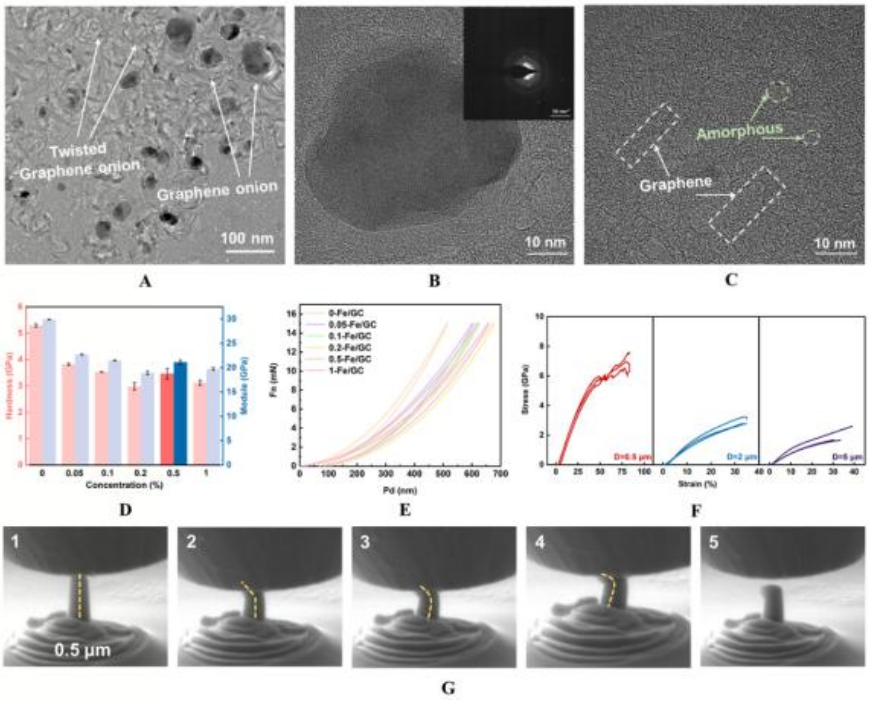

Figure 5. Microscopic morphology and mechanical property characterization of Fe/GC. A-C: Multi-scale TEM images of 0.5-Fe/GC; D: Comparison chart of nanoindentation hardness and Young's modulus of samples with different iron concentrations; E: Nanometer indentation test load-displacement curve; F: Engineering stress-strain curves of micro-columns with different diameters; G: The in-situ SEM compression evolution process of 0.5 μm diameter micro-columns.

To further evaluate the mechanical significance of the present carbon microstructure, the nanoindentation results were compared with those of representative graphite-based carbon materials reported in the literature, and the structure-property correlations within the present sample series were analyzed[1,4,39-41]. As shown in Figure 6A, the 0.5-Fe/GC sample is located in the upper-right region of the hardness-modulus map, exhibiting a superior combination of hardness and elastic modulus compared with most previously reported graphitic carbon materials. This result indicates that the present Fe-catalyzed carbon retains a relatively high local load-bearing capability despite its substantial graphitic ordering.

To clarify the structural origin of this behavior, hardness and modulus were correlated with the key structural parameters derived from the Raman and XRD analyses[42]. As shown in Figure 6B and Figure 6C, both hardness and modulus decrease with decreasing I_D/I_G, indicating that increasing structural ordering is generally accompanied by local mechanical softening. A similar trend is observed in Figure 6D and Figure 6E, where both hardness and modulus decrease with decreasing $d_{(002)}$. Since a smaller $d_{(002)}$ reflects a more compact graphitic stacking structure, these results suggest that progressive graphitic ordering and interlayer contraction tend to reduce the local resistance to elastic deformation and indentation. Such behavior is consistent with the increased tendency for basal-plane sliding in more developed graphitic structures.

Importantly, the comparison between the literature data and the present fitting results suggests that the superior micromechanical performance of 0.5-Fe/GC cannot be explained by graphitization alone. If the mechanical response were governed solely by graphitic ordering, a continuous increase in graphitization would be expected to result in simple local softening. However, the present 0.5-Fe/GC sample still maintains a remarkably high hardness-modulus combination relative to previously reported graphitic carbons. Therefore, this outstanding local mechanical performance is more reasonably attributed to the catalyst-induced topological microstructure, in which curved and structurally constrained graphitic domains help suppress facile basal-plane sliding and improve local stress transfer. In this sense, the Fe-catalyzed graphitization in the present system does not merely increase graphitic order, but generates a distinctive graphitic architecture that effectively mitigates the conventional trade-off between graphitization and micromechanical robustness.

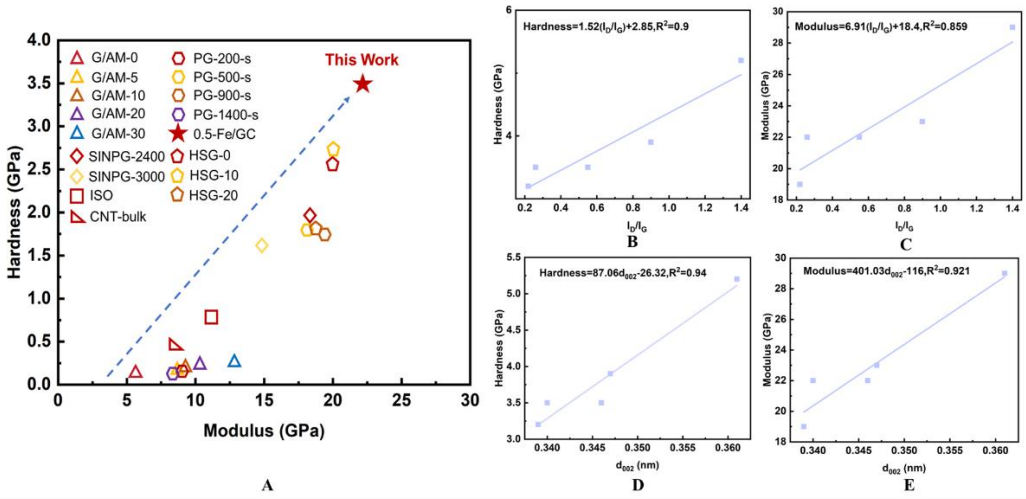

Figure 6. Comparison of nanoindentation hardness and elastic modulus in this study with representative graphite-based carbon materials reported in the literature and the structural-performance relationships obtained in this study. A: Hardness-modulus map comparing 0.5-Fe/GC with representative graphitic carbon materials from the literature; B: Correlation between elastic hardness and I_D/I_G; C: Correlation between modulus and I_D/I_G; D: Correlation between elastic hardness and $d_{(002)}$; E: Correlation between modulus and $d_{(002)}$.

CONCLUSIONS

In summary, this study develops a ferric-nitrate-mediated catalytic strategy to achieve enhanced graphitization of sugar-derived carbon at a relatively low temperature of 1,400 °C, effectively overcoming the inherent graphitization bottleneck of biomass precursors. The homogeneous incorporation of Fe species induces a unique thermal evolution pathway, promoting intensive structural reconstruction that culminates in a curved and constrained graphitic microstructure rather than a conventional lamellar arrangement. Crucially, our findings clarify that the exceptional mechanical robustness-characterized by a superior hardness-modulus combination and local compressive strength-is primarily dictated by this catalyst-induced topological architecture, which effectively suppresses facile basal-plane sliding. This work transcends the traditional objective of temperature reduction, establishing low-temperature catalytic graphitization as a sophisticated structural design strategy. It provides a robust foundation for the sustainable fabrication of high-performance biomass carbon and offers a promising route toward integrated thermo-structural carbon

blocks with enhanced mechanical durability.

DECLARATIONS

Authors' contributions

Made substantial contributions to conception and design of the study and performed data analysis and interpretation: JH.Z, DM.C, CL.W, ZH.H, A.C, YH.F, CY.W, YJ.G, H.W;

Performed data acquisition, as well as provided administrative, technical, and material support: MY.T, WZ.Z, XH.Z.

Availability of data and materials

Data will be made available on request.

AI and AI-assisted tools Statement

Not applicable.

Financial support and sponsorship

This work was supported by National Natural Science Foundation of China (Grant No. 52293372, 52502060, 52502072, 52502073), Postdoctoral Fellowship Program of CPSF (Grant No. GZB20240948), and Basic Research Program of Jiangsu (No. BK20250534, BK20250526). Wenzheng Zhang would like to express gratitude to Jiangsu Funding Program for Excellent Postdoctoral Talent. Mingyi Tan would like to thank the supported by the science foundation of national key laboratory of science and technology on advanced composites in special environments (Grant No. JCKYS2025603C007) and Science and Technology on Advanced Ceramic Fibers and Composites Laboratory (Grant No. WDZC20255290501).

Conflicts of interest

All authors declared that there are no conflicts of interest.

Consent for publication

Not applicable.

REFERENCES

1. Sun, B., D. Chen, Y. Cheng, et al., Sugar-Derived Isotropic Nanoscale Polycrystalline Graphite Capable of Considerable Plastic Deformation. *Adv Mater,* 2022. **34**(31): p. e2200363.[DOI: 10.1002/adma.202200363]

2. Zhang, W., M. Tan, D. Chen, et al., Sugar-Derived Nanocrystalline Graphite Matrix C/C Composites with Excellent Ablative Resistance at 3000 degrees C. *Adv Mater,* 2024. **36**(7): p. e2309899.[DOI: 10.1002/adma.202309899]

3. Li, J., J. Liu, N. Li, et al., High thermal conductivity graphene-based interfacial materials through oriented assembly and catalytic graphitization for thermal management. *Carbon,* 2025. **235**.[DOI: 10.1016/j.carbon.2025.120081]

4. Li, J.L., L. Wang, T. He, et al., Surface graphitization and mechanical properties of hot-pressed bulk carbon nanotubes compacted by spark plasma sintering. *Carbon,* 2007. **45**(13): p. 2636-42.[DOI: 10.1016/j.carbon.2007.08.023]

5. Zhu, F., W.L. Song, J. Ge, et al., High-Purity Graphitic Carbon for Energy Storage: Sustainable Electrochemical Conversion from Petroleum Coke. *Adv Sci (Weinh),* 2023. **10**(8): p. e2205269.[DOI: 10.1002/advs.202205269]

6. Wang, L., T. Qiu, Z. Guo, et al., Changes and Migration of Coal-Derived Minerals on the Graphitization Process of Anthracite. *ACS Omega,* 2021. **6**(1): p. 180-7.[DOI: 10.1021/acsomega.0c04120]

7. Hou, C., D. Chen, M. Tan, et al., Lightweight and High-Strength Carbon Bulk Preparation Via Low-Temperature Pressureless Sintering of Sugar-Derived Carbon. *Adv Sci (Weinh),* 2026. **13**(7): p. e18437.[DOI: 10.1002/advs.202518437]

8. Chen, J., H. Zhang, B. Li, et al., Confined graphitization induced pore generation for designing novel potassium-ion battery carbon anode with large capacity and ultra-long cycle life. *Carbon,* 2024. **229**.[DOI: 10.1016/j.carbon.2024.119511]

9. Yang, Y., D. Chen, Y. Cheng, et al., Eco-friendly and sustainable approach of

assembling sugars into biobased carbon fibers. *Green Chemistry,* 2022. **24**(13): p. 5097-106.[DOI: 10.1039/D2GC01075E]

10. Zhao, X., Y. Ding, Q. Xu, et al., Low-Temperature Growth of Hard Carbon with Graphite Crystal for Sodium-Ion Storage with High Initial Coulombic Efficiency: A General Method. *Advanced Energy Materials,* 2019. **9**(10).[DOI: 10.1002/aenm.201803648]

11. Hunter, R.D., J. Ramírez-Rico, and Z. Schnepp, Iron-catalyzed graphitization for the synthesis of nanostructured graphitic carbons. Journal of Materials *Chemistry A,* 2022. **10**(9): p. 4489-516.[DOI: 10.1039/D1TA09654K]

12. Gomez-Martin, A., Z. Schnepp, and J. Ramirez-Rico, Structural Evolution in Iron-Catalyzed Graphitization of Hard Carbons. *Chemistry of Materials,* 2021. **33**(9): p. 3087-97.[DOI: 10.1021/acs.chemmater.0c04385]

13. Thompson, E., A.E. Danks, L. Bourgeois, et al., Iron-catalyzed graphitization of biomass. *Green Chemistry,* 2015. **17**(1): p. 551-6.[DOI: 10.1039/C4GC01673D]

14. Li, H., H. Zhang, K. Li, et al., Catalytic graphitization of coke carbon by iron: Understanding the evolution of carbon Structure, morphology and lattice fringes. *Fuel,* 2020. **279**.[DOI: 10.1016/j.fuel.2020.118531]

15. Jeong, H., J.A. Kim, S.H. Lee, et al., Iron-catalyzed graphitization of lignocellulose: A pathway to develop artificial graphite as anode materials for lithium-ion batteries applications. *Journal of Alloys and Compounds,* 2025. **1020**.[DOI: 10.1016/j.jallcom.2025.179485]

16. Goldie, S.J., S. Jiang, and K.S. Coleman, Cobalt nanoparticle catalysed graphitization and the effect of metal precursor decomposition temperature. *Materials Advances,* 2021. **2**(10): p. 3353-61.[DOI: 10.1039/D1MA00125F]

17. Jurkiewicz, K., B. Liszka, P. Gancarz, et al., Sucrose-Based Dense, Pure, and Highly-Crystalline Graphitic Materials for Lithium-Ion Batteries. *Advanced Functional Materials,* 2024. **34**(51).[DOI: 10.1002/adfm.202410409]

18. You, H., J. Hui, Y. Zhou, et al., Sustainable Production of Biomass-Derived Graphite and Graphene Conductive Inks from Biochar. *Small,* 2024. **20**(52): p. e2406669.[DOI:

10.1002/smll.202406669]

19. Tan, M., D. Chen, Y. Cheng, et al., Anisotropically Oriented Carbon Films with Dual-Function of Efficient Heat Dissipation and Excellent Electromagnetic Interference Shielding Performances. *Advanced Functional Materials,* 2022. **32**(31).[DOI: 10.1002/adfm.202202057]

20. Wu, S., D. Chen, W. Han, et al., Ultralight and hydrophobic MXene/chitosan-derived hybrid carbon aerogel with hierarchical pore structure for durable electromagnetic interference shielding and thermal insulation. *Chemical Engineering Journal,* 2022. **446**.[DOI: 10.1016/j.cej.2022.137093]

21. Yang, Y., D. Chen, W. Han, et al., Nature-inspired self-activation method for the controllable synthesis of highly porous carbons for high-performance supercapacitors. *Carbon,* 2023. **205**: p. 1-9.[DOI: 10.1016/j.carbon.2023.01.013]

22. Corbin, J.C., B. Sierau, M. Gysel, et al., Mass spectrometry of refractory black carbon particles from six sources: carbon-cluster and oxygenated ions. *Atmospheric Chemistry and Physics,* 2014. **14**(5): p. 2591-603.[DOI: 10.5194/acp-14-2591-2014]

23. Nishioka, T., T. Kasama, T. Kinumi, et al., Winners of CASMI2013: Automated Tools and Challenge Data. *Mass Spectrom (Tokyo),* 2014. **3**(Spec Iss 2): p. S0039.[DOI: 10.5702/massspectrometry.S0039]

24. Hunter, R.D., M. Takeguchi, A. Hashimoto, et al., Elucidating the Mechanism of Iron-Catalyzed Graphitization: The First Observation of Homogeneous Solid-State Catalysis. *Adv Mater,* 2024. **36**(36): p. e2404170.[DOI: 10.1002/adma.202404170]

25. Vilas-Boas, A.C.M., L.A.C. Tarelho, H.S.M. Oliveira, et al., Valorisation of residual biomass by pyrolysis: influence of process conditions on products. *Sustainable Energy & Fuels,* 2024. **8**(2): p. 379-96.[DOI: 10.1039/D3SE01216F]

26. Dreimol, C.H., H. Guo, M. Ritter, et al., Sustainable wood electronics by iron-catalyzed laser-induced graphitization for large-scale applications. *Nat Commun,* 2022. **13**(1): p. 3680.[DOI: 10.1038/s41467-022-31283-7]

27. Peng, H., X. Ming, K. Pang, et al., Highly electrically conductive graphene papers via catalytic graphitization. *Nano Research,* 2022. **15**(6): p. 4902-8.[DOI:

10.1007/s12274-022-4130-z]

28. Zickler, G.A., B. Smarsly, N. Gierlinger, et al., A reconsideration of the relationship between the crystallite size La of carbons determined by X-ray diffraction and Raman spectroscopy. *Carbon,* 2006. **44**(15): p. 3239-46.[DOI: 10.1016/j.carbon.2006.06.029]

29. Badenhorst, H., Microstructure of natural graphite flakes revealed by oxidation: Limitations of XRD and Raman techniques for crystallinity estimates. *Carbon,* 2014. **66**: p. 674-90.[DOI: 10.1016/j.carbon.2013.09.065]

30. Iwashita, N., C.R. Park, H. Fujimoto, et al., Specification for a standard procedure of X-ray diffraction measurements on carbon materials. *Carbon,* 2004. **42**(4): p. 701-14.[DOI: 10.1016/j.carbon.2004.02.008]

31. Qiu, C., L. Jiang, Y. Gao, et al., Effects of oxygen-containing functional groups on carbon materials in supercapacitors: A review. *Materials & Design*, 2023. **230**.[DOI: 10.1016/j.matdes.2023.111952]

32. Yoon, J.C., X. Dai, K.N. Kang, et al., Graphitization with Suppressed Carbon Loss for High-Quality Reduced Graphene Oxide. *ACS Nano,* 2021. **15**(7): p. 11655-66.[DOI: 10.1021/acsnano.1c02178]

33. Goldie, S.J. and K.S. Coleman, Graphitization by Metal Particles. *ACS Omega,* 2023. **8**(3): p. 3278-85.[DOI: 10.1021/acsomega.2c06848]

34. Garcia, A.B., I. Camean, I. Suelves, et al., The graphitization of carbon nanofibers produced by the catalytic decomposition of natural gas. *Carbon,* 2009. **47**(11): p. 2563-70.[DOI: 10.1016/j.carbon.2009.04.047]

35. Wang, R., G. Lu, W. Qiao, et al., Catalytic Graphitization of Coal-Based Carbon Materials with Light Rare Earth Elements. *Langmuir,* 2016. **32**(34): p. 8583-92.[DOI: 10.1021/acs.langmuir.6b02000]

36. Kabel, J., T.E.J. Edwards, A. Sharma, et al., Direct observation of the elasticity-texture relationship in pyrolytic carbon via in situ micropillar compression and digital image correlation. *Carbon,* 2021. **182**: p. 571-84.[DOI: 10.1016/j.carbon.2021.06.045]

37. Rossi, E., J. Bauer, and M. Sebastiani, Humidity-dependent flaw sensitivity in the

crack propagation resistance of 3D-printed nano-ceramics. *Scripta Materialia,* 2021. **194**.[DOI: 10.1016/j.scriptamat.2020.113684]

38. Zhang, N., D. Huang, H. Quan, et al., Unveiling the microscopic compression failure behavior of mesophase-pitch-based carbon fibers for improving the compressive strength of their polymer composites. *Composites Part B: Engineering,* 2024. **283**.[DOI: 10.1016/j.compositesb.2024.111658]

39. Chen, W., J. Sheng, D. Chen, et al., Graphene-amorphous carbon with interwoven networks for enhanced strength. *Nat Commun,* 2025. **16**(1): p. 10513.[DOI: 10.1038/s41467-025-65877-8]

40. Liang, Z., M. Ma, Y. Zhou, et al., Amorphous carbon reinforced graphite combining high strength and superior electrical conductivity. *Carbon,* 2025. **244**.[DOI: 10.1016/j.carbon.2025.120651]

41. Zhang, Q., J. Fang, W. Ma, et al., Interlocking reinforced graphitic material based on nanodiamond-derived nano-onion-helical carbon nanotube anchored structure. *Diamond and Related Materials,* 2025. **157**.[DOI: 10.1016/j.diamond.2025.112518]

42. Shirasu, K., K. Goto, and K. Naito, Microstructure-elastic property relationships in carbon fibers: A nanoindentation study. *Composites Part B: Engineering,* 2020. **200**.[DOI: 10.1016/j.compositesb.2020.108342]